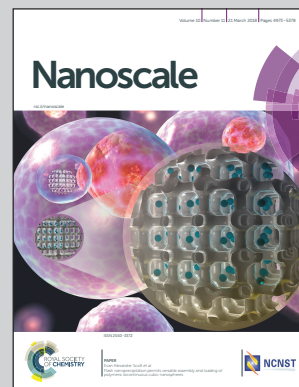


Showcasing research from the Institute of Modern Optics, Nankai University, Key Laboratory of Optical Information Science and Technology, Ministry of Education, Tianjin, China.

An on-chip hybrid plasmonic light steering concentrator with ~96% coupling efficiency

A hybrid photonic-plasmonic device based on a metal-dielectric-metal sandwich structure achieves the steering and nanofocusing of light waves simultaneously by the on-chip surface plasmon polariton excitation of TE-polarized light. The designed configuration overcomes the inherent ohmic losses of the metal, greatly improving the nanofocusing efficiency of the device and ensuring significant local-field enhancement. These outstanding optical performances of the device provide gigantic potential for all-optical information processing, optical manipulation and plasma-assisted functional elements in highly integrated polarization-free photonic circuits.

As featured in:



See Dong Xiang *et al.*, *Nanoscale*, 2018, 10, 5097.



rsc.li/nanoscale

Registered charity number: 207890



Cite this: *Nanoscale*, 2018, **10**, 5097

An on-chip hybrid plasmonic light steering concentrator with ~96% coupling efficiency†

Tian Zhang,^a Maoning Wang,^a Yong Yang,^a Fei Fan,^a Takhee Lee,^b Haitao Liu^a and Dong Xiang *^a

We, for the first time, propose and theoretically study a plasmonic light steering concentrator (PLSC) that is based on a hybrid photonic–plasmonic sandwich structure. In this device, a transverse electric (TE) polarization guided mode supported by a silicon-on-insulator (SOI) waveguide is vertically coupled to a metal–dielectric–metal sandwich structure, while the structure steers the light to a perpendicular metal taper and focuses the light on the apex of the taper with a small radius of 15 nm. Based on the coupled-mode theory, the two supermodes (quasi-TM modes) are clarified to illustrate the coupling mechanism of the device. We numerically obtain over 96% coupling efficiency at the 1500 nm telecommunication wavelength, and the mode width supported by the apex is limited laterally within the range of ~110 nm, where the field enhancement calculated is found to be more than 10^7 compared to that of light in the silicon waveguide.

Received 9th January 2018,
Accepted 31st January 2018

DOI: 10.1039/c8nr00213d

rsc.li/nanoscale

Introduction

Plasmonic nanostructures have stimulated tremendous interest in the fields of nanotechnology and biosensing due to their remarkable capabilities of field enhancement and extreme sensitivity to changes in the surrounding environment.^{1,2} In view of this, there have been two mainstream mechanisms to explain the powerful ability of plasmonic nanostructures. One of the explanations is based on surface plasmon polaritons (SPPs), which are transverse-magnetic (TM) waves that are bound to and propagate along the metal/dielectric interface.³ SPPs can be used to perform nanofocusing beyond the diffraction limit, thus achieving the maximum enhancement of the local field.^{4–6} The advantages of SPPs can be applied to a variety of nano-optical fields in the future, including optical trapping,⁷ telecommunication,⁸ and nanolasers.⁹ However, because of the inherent polarization dependence of SPPs,^{1,3,4} it is almost impossible to excite SPPs with TE polarized incident light (the magnetic vector is perpendicular to that of the SPPs), thus achieving the polarization-free excitation of SPPs is crucial for its practical application. Moreover, due to the high

intrinsic ohmic loss of noble metals,¹⁰ the integrated application of plasmonic nanostructures is limited.

Another explanation for the powerful abilities of plasmonic nanostructures is localized surface plasmon resonance (LSPR), which is caused by the collective oscillation of free electrons on the surface of metal nanoparticles in resonance with the incident light field at a particular frequency.¹¹ The intrinsic properties of the LSPR have led to a strong near-field enhancement, which has laid the foundation for practical applications, including super-resolution optical imaging,¹² LSPR sensing,^{13,14} spectroscopy based on surface enhanced Raman scattering (SERS),¹⁵ single-molecule fluorescence techniques¹⁶ and nonlinear optics.^{17,18} Due to the diffraction limit, the free-space excitation light spot cannot be coupled with the individual nanoparticles efficiently, so intricate and expensive optical equipment is required to excite the device and detect the signal.¹⁹

To cope with this bottleneck, a series of novel hybrid photonic–plasmonic (HPP) structures have been reported recently to address the propagation loss of plasmonic structures and the inefficient coupling problem in free space.^{20–36} A typical HPP structure is usually composed of a metal plasmonic nanostructure and a dielectric photonic waveguide, and a low-refractive-index dielectric material such as silica (SiO₂) is sandwiched between them. In 2011, He *et al.* designed an on-chip nanofocuser by tapering a coupled photonic–plasmonic waveguide based on the vertical side coupling between a silicon-on-insulator (SOI) waveguide and a gold nanostrip.²⁴ Under the excitation of 1550 nm TM light, a vertical coupling efficiency of ~50% was achieved, and an enhancement of electric field (50-fold) was realized in the focus region of size 20 nm ×

^aInstitute of Modern Optics, Nankai University, Key Laboratory of Optical Information Science and Technology, Ministry of Education, Tianjin 300350, China. E-mail: xiangdongde@126.com

^bDepartment of Physics and Astronomy, and Institute of Applied Physics, Seoul National University, Seoul 08826, Korea

† Electronic supplementary information (ESI) available: S1: Description of the material; S2: Coupling between the silver strips; S3: Loss mode and back reflection. See DOI: 10.1039/c8nr00213d

20 nm × 7 nm by numerical calculation. Two years later, Chamanzar *et al.* presented an on-chip LSPR sensor that efficiently couples light waves from the dielectric waveguides to the LSPR nanoparticles by integrating individual nanorods on top of a silicon nitride (Si₃N₄) waveguide.²⁹ By combining the device with the microfluidic system, a sensitivity of approximately 250 nm per RIU was realized, while the coupling efficiency of the device was ~9.7%. In 2014, Osowiecki *et al.* demonstrated a plasmonic slot waveguide cavity (PSWC) sensor that vertically couples the guided mode in the silicon (Si) photonic waveguide to the plasmonic cavity isolated by the SiO₂ buffer layer, which results in a significant enhancement of the electric field in the plasmonic cavity.³⁰ In 2015, Luo *et al.* reported the realization of a novel plasmonic light concentrator (PLC) by placing a triangular gold wedge structure over a sufficiently long Si waveguide, coupling the light wave from the Si waveguide to the plasmonic nanotaper and focusing it at the apex.³¹ Under the excitation of 1550 nm TM light, the device achieved 92% side coupling efficiency, and a large field concentration factor of ~4.9 was obtained at the apex of the nanotaper with a radius of 20 nm experimentally. Apart from these structures, the recently proposed hybrid configurations that combine metallic nanowire plasmon polaritons with dielectric waveguides (SOI WGs) have attracted intensive attention, which can be exploited for high-performance light transport and nanofocusing.^{37,38} Noteworthy, for the silicon-based photonic integrated platform, transverse-electric (TE) polarized light has more advantages because of its unique confinement.³³ To the best of our knowledge, no such TE-light-based on-chip nanofocuser has been reported so far.

In this paper, we present a novel hybrid plasmonic light steering concentrator (PLSC) that is designed to achieve efficient vertical coupling between optical waves and SPPs by placing a metal–dielectric–metal sandwich taper structure at the top of the silicon photonic waveguide, while the coupled light energy is steered and focused on the apex along the plasmonic taper structure. Under the excitation with 1500 nm TE-polarized light, the device achieves the enhancement of field amplitude by a factor of more than 10⁷ compared to that of light in the silicon photonic waveguide at the apex of radius 15 nm with a coupling efficiency of over 96%. We believe that the proposed structure provides an alternative approach for all-optical information processing and optical manipulation in highly integrated plasmonic circuits.

PLSC structure

The basic structure of the device consists of a dielectric waveguide and a metal–dielectric–metal sandwich metal taper located at its top, as shown in Fig. 1(a). In this study, we use a low-loss silver strip as the plasmonic material to reduce the absorption loss caused by the metal. The dielectric photonic waveguide is made of silicon, and silica is used as the substrate material. Unlike in traditional methods, the silica material is not used as a buffer layer between the waveguide

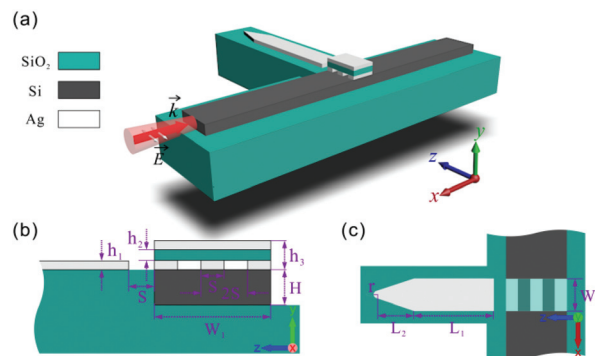


Fig. 1 (a) A schematic diagram of an integrated PLSC in which a sandwich silver taper structure is laid on top of a silicon waveguide. (b) Side view of the integrated structure. (c) Top view of the integrated structure.

and plasmonic structure in our device to minimize the coupling length.³⁰ The surrounding material that wraps the structure is air. Here, the thickness of the silicon waveguide H is set to 170 nm and the width of this waveguide W_1 is set to 630 nm, to maximize the incident light to the waveguide. Due to the design of the spatial dimensions of the silicon waveguide, only the fundamental quasi-TE mode is supported in the infrared wavelength range between 1000 nm and 2000 nm. In addition, we set up the coordinate system. In this coordinate system, the $x = 0$ plane passes vertically through the middle part of the silver taper, the $y = 0$ plane passes horizontally through the middle part of the taper, and the $z = 0$ plane passes vertically through the centre of the apex with a radius of 15 nm.

Fig. 1(b) shows a side view of the structure, in which the thickness of the silver strip is 30 nm, to make a trade-off between the field localization and the ohmic loss.⁶ The top silver layer with a thickness $h_3 - (h_2 + h_1)$ of 30 nm is designed to suppress unwanted radiation. The thickness of the silica layer h_2 sandwiched between silver layers is a variable parameter, by which the coupling efficiency of the device is mainly determined. The equal spacing S between silver strips is determined by the number N of silver strips, *i.e.*, $S = W_1/(2N - 1)$. The gap size between the metal taper and the sandwich structure is designed to be S also. Fig. 1(c) shows a top view of the structure. Here, W_2 denotes the length of a silver strip, which is designed according to the coupling length. The length L_1 between the sandwich structure and the silver taper should be long enough to suppress the leaky mode and radiation mode caused by the periodic structure. Here, $L_1 = 1600$ nm. We use L_2 to denote the length of the taper, which is mainly determined by the vertex angle of the taper. Here, the 60° vertex angle is adopted for the calculation of the transmission spectrum. To make the fabrication process easier, the apex of the silver taper is rounded to a curvature radius of 15 nm, so that the width of the narrowest portion of the taper is equal to the thickness of the deposited silver layer.

To understand the role of the variable parameters in determining the performance of the hybrid device, we calculated

the transmission spectrum of the device. We first calculated the effects of silver strips with different lengths on the transmission spectrum of the device. Subsequently, we studied the impact of the thickness of the sandwiched silica on the transmission spectrum. The commercial software CST Microwave Studio was used to simulate the transmission spectrum of forward wave $|S_{21}|^2$ in dB, where the left port of the waveguide is defined as port 1, and the right port of the waveguide is defined as port 2. To ensure the accuracy of the simulation results, a three-dimensional hexahedral mesh is adopted, in which the minimum mesh size is 5 nm. Eventually, 3 billion mesh cells are generated in the bounding box of size $6.4 \mu\text{m}$ (x) \times $1.3 \mu\text{m}$ (y) \times $4.9 \mu\text{m}$ (z). The excitation source is a 25 fs pulse that uses a frequency range from 0.15 PHz (2000 nm) to 0.3 PHz (1000 nm). In the simulation, the open boundary condition (perfectly matched layer) was adopted. The permittivity of silver was obtained by fitting the optical constants provided by Johnson and Christy³⁹ (see S1 of the ESI†).

Fig. 2(a) shows the relationship between the transmission spectrum and the length of the cavity formed by the silver strip. It is observed that the transmission dip is highly dependent on the cavity length. When the cavity length is less than 300 nm, as marked by the horizontal dotted line in Fig. 2(a), the transmission value is quite high and no obvious transmission dip is observed over the entire frequency range. This observation is reasonable since the cavity length is too short to reach the coupling length. When the cavity length is longer than the coupling length, multiple transmission dips appear, and the main transmission dip is more impressive than that corresponding to the coupling length due to the beat effect.³¹

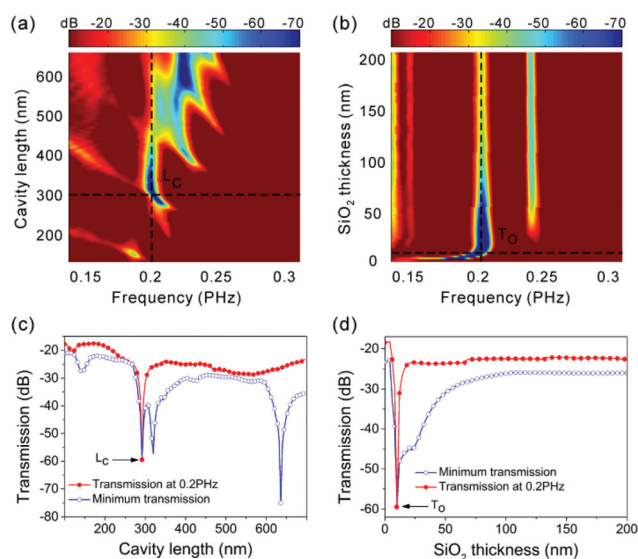


Fig. 2 (a) Dependence of transmission spectrum on the length of the cavity formed by the silver strip (W_2), where the thickness of the top silver plate is 30 nm. (b) Dependence of transmission spectrum on the thickness of the silica layer, where the length of the cavity consisting of silver strips is 300 nm. Effect of (c) silver strip length and (d) silica thickness on transmittance at fixed frequency (0.2 PHz) and full frequency range.

The intersection (L_C) of two black dashed lines in Fig. 2(a) represents the minimum transmission of 0.2 PHz (1500 nm) light when the length of the silver strip reaches the coupling length (the light was mainly coupled to the top plasmonic structure). The red line in Fig. 2(c) denotes the transmission as a function of cavity length for a 1500 nm light source, which also corresponds to the transmission marked by the vertical dotted line in Fig. 2(a). The blue line denotes the minimum transmission across the full frequency regime. It is worth noting that when the length of the silver strip is about $2L_C$, the transmission is smaller than that at L_C , which is caused by the beat effect.

Fig. 2(b) shows the relationship between the transmission spectrum and the thickness of silica. When the thickness increases gradually, the transmission dip becomes increasingly significant. The optimal dip appears at the position $h_2 = 10$ nm, as marked by the horizontal dotted line in this figure. When the optimum thickness is exceeded, the transmission spectrum exhibits multiple dips and the positions of the transmission dips remain substantially independent of the SiO₂ thickness. The radiation in the vertical direction can be greatly suppressed by the top silver layer only when the sandwich structure is at its optimum thickness. Similarly, the intersection (T_O) of the two black dashed lines in Fig. 2(b) (*i.e.*, the intersection of the blue and red curves in Fig. 2(d)) represents the minimum transmission corresponding to the optimum thickness. In view of the above calculation results, for the sandwich structure with three silver strips, we opted for the following parameters: the length of the silver strips $W_2 = 300$ nm, the thickness of the silica layer $h_2 = 10$ nm, and other parameters as mentioned earlier.

Mode analysis of the HPP sandwich structure

To control the PLSC more effectively, we needed to carry out an in-depth study of the functional mode in the hybrid photonic-plasmonic sandwich structure. The sandwich structure on the silicon waveguide consists of two silver layers and a sandwiched silica layer. The bottom silver layer possesses a certain periodic structure and the top silver layer is a metal plate, as shown in Fig. 1. According to the calculation results above, here, the thickness of silica is 10 nm, the thickness of the two silver layers is 30 nm, and the spacing between silver strips is 126 nm. The cross-sectional dimension of the silicon photonic waveguide is set to $630 \text{ nm} \times 170 \text{ nm}$, which is consistent with the previous one and is intended to support the operation of the single fundamental quasi-TE mode. The hybrid photonic-plasmonic sandwich structure is placed in ambient air, which has a refractive index of 1.

First, the periodic silver strips in the HPP structure are considered as a whole (the coupling between the silver strips is not considered). As shown in Fig. 3(a), we first analyse the quasi-TE mode (denoted as TE₀) in the pure photonic waveguide (without the HPP structure), and then we analyse the uncoupled asymmetric mode (denoted as A₀) of the pure

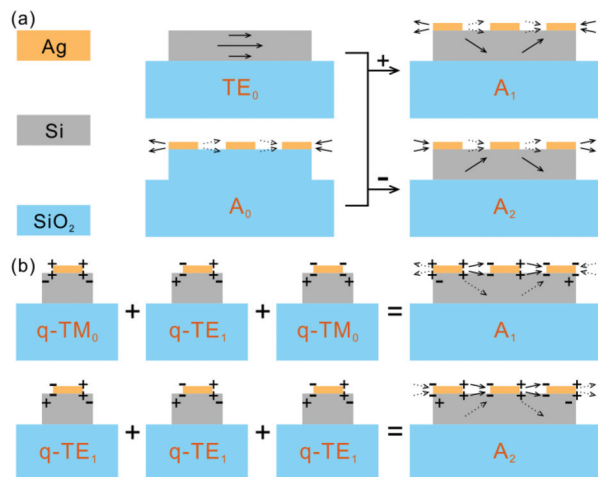


Fig. 3 (a) Supermode analysis of periodic silver strips as a whole. The two supermodes (A_1 and A_2) come from the superposition of the quasi-TE mode (TE_0) of the pure photonic waveguide and the uncoupled asymmetric mode (A_0) of the pure plasmonic waveguide. (b) Schematic drawing of substrate-mediated coupling between silver strips. Two supermodes (asymmetric modes A_1 , A_2) generated by the anti-phase coupling between quasi-modes ($q-TM_0$ and $q-TE_1$). The solid and dashed arrows depict the electric-field direction and the coupling between the individual silver strips, respectively.

plasmonic waveguide (using silica to replace silicon). Finally, we use the supermode analysis to obtain two hybrid photonic-plasmonic waveguide modes (denoted as A_1 and A_2) by superimposing the modes of the two structures.

Subsequently, an “image charge” picture in the quasi-static limit⁴⁰ is utilized to analyse the mutual coupling of silver strips shown in Fig. 3(b). For the two independent quasi-modes, $q-TM_0$ and $q-TE_1$, which exist at a frequency of 0.2 PHz, four supermodes (asymmetric modes A_1 , A_2 and symmetric modes S_1 , S_2) can be generated by the anti-phase coupling (inducing the opposite polarized charges on the substrate surface, see Fig. 3(b)) and in-phase coupling (inducing the same polarized charges on the substrate surface, see S2 of the ESI† for details) between them. Therefore, for TE-polarized incident light, only two asymmetric modes are present during the coupling process. The analytical results produced by the two different methods (see Fig. 3(a) and (b)) agree well with each other, indicating the validity of our analysis.

Finally, the finite element method (FEM, COMSOL Multiphysics) is used to perform the mode analysis for the HPP structure at wavelength $\lambda = 1500$ nm. In order to ensure the accuracy of the calculation results, the convergence test is performed through mesh refinement. In our simulation, a perfectly matched layer is employed to simulate the infinite air and substrate. The refractive index of the silicon substrate at the corresponding wavelength was obtained by fitting the refractive index data taken from Green.⁴¹ The refractive index of silica used here is 1.5.⁴² Similarly, the frequency-dependent permittivity of silver was calculated by polynomial fitting of the experimental data of the measured permittivity (see S1 of

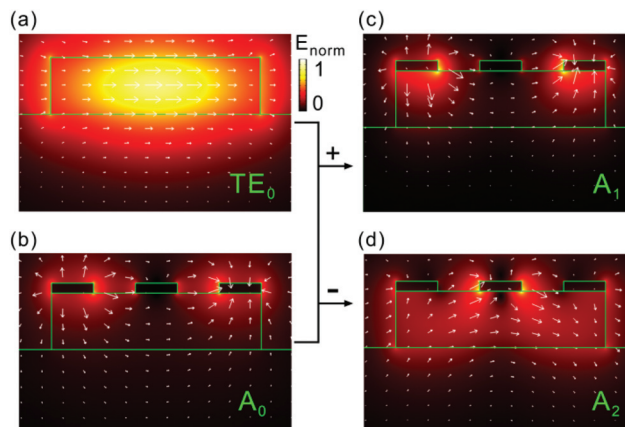


Fig. 4 The normalized electric-field profiles of (a) TE_0 , (b) A_0 , (c) A_1 and (d) A_2 . The analysis wavelength is 1500 nm. The electric-field directions of the modes are indicated by arrows.

the ESI†).³⁹ Fig. 4 shows the normalized electric-field profiles for the modes TE_0 , A_0 , A_1 and A_2 . The electric-field direction is plotted to facilitate a more accurate understanding of the whole mode-coupling process. It is noteworthy that the electric-field distribution shown in Fig. 4(c and d) indicates that the two supermodes generated by the coupling of the TE_0 mode in the silicon photonic waveguide through the HPP structure can be considered as quasi-TM modes. Therefore, the incident TE polarized light wave can be coupled to a surface plasmon under the mediation of the HPP structure.

In order to suppress the energy leaked into air, we further added a silver plate on the top of the previous HPP structure to form a new HPP sandwich structure, as shown in Fig. 5(a). A side view of the $x = 0$ plane of the structure is shown in Fig. 5(b). The normalized electric-field profiles presented in Fig. 5(c and d) do increase considerably compared to the results in Fig. 4(c and d). However, the new HPP sandwich structure also results in an additional loss mode A_L (see S3 of the ESI†) because the supermode A_1 and A_2 have two different effective indices, which results in interference during the whole coupling process. Therefore, based on the coupled-mode theory,⁴³ energy transfers back and forth between the two supermodes when the length of the silver strip equals the coupling length. The real part of the mode effective index can be calculated using $\text{Re}(n_{\text{eff}}) = \text{Re}(\beta/k_0)$, where β is the propagation constant of SPPs, and k_0 is the free space wave vector. Therefore, the coupling length L_C based on the coupled-mode theory caused by the interference between different modes in the HPP structure can be calculated by the following formula

$$L_C = \frac{\lambda_0}{2|n_{A_2} - n_{A_1}|} \quad (1)$$

where n_{A_2} and n_{A_1} are the effective indices of two different supermodes, respectively, and λ_0 is the free space wavelength. For the sandwich structure, the effective indices of the two supermodes A_1 and A_2 at the wavelength of 1500 nm are 4.5386 and 2.2501, respectively, so that the coupling length of

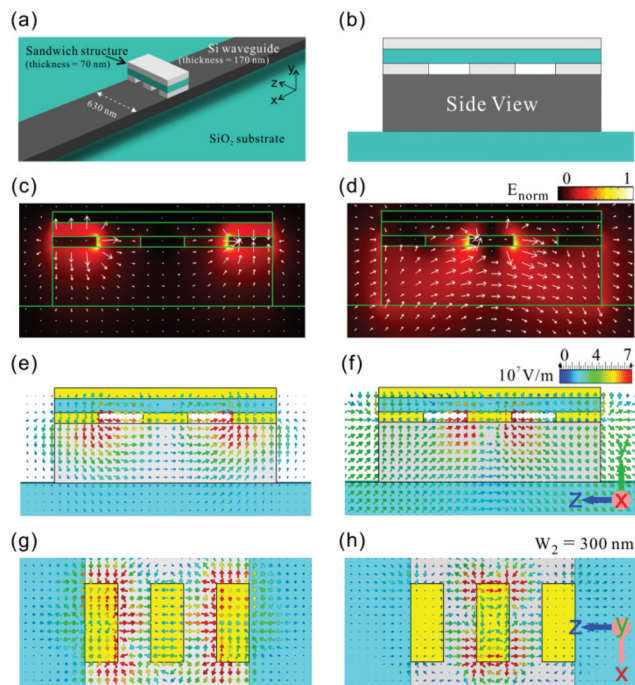


Fig. 5 (a) Schematic diagram and (b) side view of the HPP sandwich structure. The normalized electric-field profiles of (c) A_1 and (d) A_2 obtained through mode analysis. The electric-field distribution of (e) A_1 and (f) A_2 in the $x = 0$ plane through a full-wave simulation of the HPP sandwich structure. The electric-field distribution of (g) A_1 and (h) A_2 in the $y = 0$ plane.

the structure can be calculated to be about 328 nm. The electric-field distribution in the $x = 0$ plane of the full-wave simulated HPP sandwich structure confirms the argument that energy transfers between the two supermodes (A_1 and A_2), see Fig. 5(e and f). Fig. 5(g and h) also show the electric-field distribution of the two supermodes of the $y = 0$ plane, where the length of the silver strip is ~ 300 nm. This is consistent with the coupling length L_C that was calculated using eqn (1). In addition, it can be seen from the electric field distribution shown in Fig. 5(g and h) that the two supermodes undergo a beat effect due to their different effective indices, where the beat length is equal to the half of coupling length.

Minimizing the coupling length of the HPP structure can save as much space as possible for the layout of the circuitry in the integrated photonic circuit and therefore it is of great importance. In Fig. 6(a), we show the calculated coupling lengths of silver strips with different spacings in the HPP structure (the top silver plate does not exist) and the HPP sandwich structure (the top silver plate exists). For both structures, the coupling length becomes longer as the spacing (period of the silver strip) increases, which is determined by the matching condition.⁴⁴ From the matching condition, the increase of the spacing between the periodic silver strips leads to a decrease of the propagation constant β of SPPs (other parameters remain unchanged), which is reflected in the decrease of the difference between the effective indices of the two super-

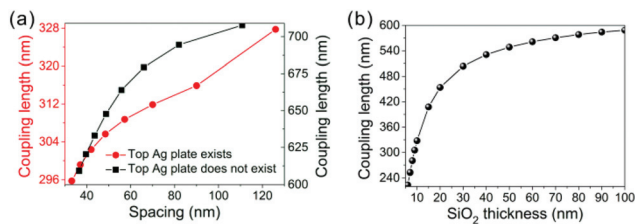


Fig. 6 (a) The coupling lengths of silver strips with different spacing in the HPP structure (the top silver plate does not exist) and the HPP sandwich structure (the top silver plate exists). (b) The dependence of the coupling length on the silica thickness (silver plate height), where the structure contains three silver strips.

modes in eqn (1), so that the coupling length becomes longer. Moreover, the existence of the silver plate makes the scale of the coupling length greatly reduced, this phenomenon is due to the increase of the diffraction order caused by the suppressed radiation and makes the propagation constant β of SPPs increase, so that the denominator in eqn (1) increases eventually leading to a decrease of the coupling length. In principle, the greater the distance between the top silver plate and the periodic silver strip, the smaller the diffraction order, and the longer the coupling length, which eventually coincides with the coupling length in the HPP structure (the top silver plate does not exist). This analysis is confirmed by the theoretical calculation shown in Fig. 6(b), which also confirms the correctness of our interpretation of the coupling mechanism.

As discussed, the periodic silver strip compensates for the momentum mismatch,⁴⁴ which provides a feasible solution for the SPP excitation. That is, a beam of TE-polarized light waves incident from the left end of the waveguide is coupled into the HPP sandwich structure to produce two quasi-TM modes (here, we denote them as A_1 and A_2 , respectively), which play a crucial role in the excitation process of SPPs. When the length of the silver strip is equal to the coupling length, the matching condition can be extremely satisfied, and the coupling efficiency of the sandwich structure is maximized, so the SPPs can also be greatly excited. Compared with the previous experimental results,⁶ when a metal taper is added on the side, the SPPs excited from the HPP sandwich structure can propagate along its edge and eventually achieve nanofocusing at the apex.

Coupling efficiency of the PLSC

As mentioned earlier, we combined an on-chip taper with a hybrid photonic-plasmonic sandwich structure to form a PLSC in which the substrate material carrying the taper is silica so that the light can be better confined to the silicon photonic waveguide spread. Then we performed a numerical simulation of the PLSC device. The calculated transmission spectra and coupling efficiency of the device are shown in Fig. 7. The coupling efficiency of the device is defined as $\eta = (P_t - P_o - P_l - P_r)/P_t$, where P_t is the total incident power, P_o is the output power, P_l is the power of the loss mode, and P_r is

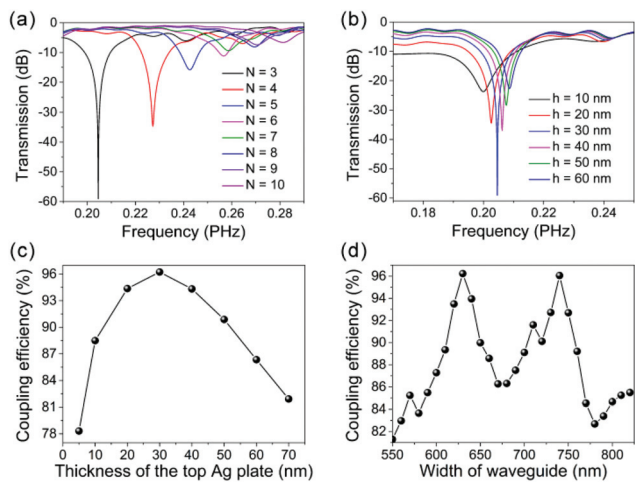


Fig. 7 (a) The transmission spectra of the PLSC with different numbers of silver strips when the on-chip taper is taken into account. (b) Transmission spectra of PLSC with different thicknesses of the top silver plate, where $N = 3$. (c) The coupling efficiency of PLSCs with different thicknesses of the top silver plate. (d) Dependence of coupling efficiency of the PLSC on the width of the silicon photonic waveguide.

the power of back reflection. Power can be calculated by the formula

$$P = \iint \langle \mathbf{S} \rangle \cdot \hat{\mathbf{x}} dydz \quad (2)$$

where $\langle \mathbf{S} \rangle = (1/2)\text{Re}(\mathbf{E} \times \mathbf{H}^*)$ is the time-averaged Poynting vector.⁴⁵

Fig. 7(a) shows the transmission spectra of the PLSC with different numbers of silver strips when the on-chip taper is taken into account. It was found that as the number of silver strips decreases, the extinction ratio of the device becomes more pronounced. The extinction ratio of 60 dB is obtained at about 1500 nm when the number of silver strips is three. As discussed earlier, the more the number of silver strips, the more generated modes, which can result in a poor coupling efficient for a system with a specific mode requirement. We further calculate the transmission spectra of PLSC as a function of the thickness of the top silver plate in the range of 0.15 PHz (2000 nm) to 0.3 PHz (1000 nm) when the spacing $S = 126$ nm is fixed. As can be seen from Fig. 7(b), with the increase of silver plate thickness, the minimum transmission of the device first decreases and then increases. This is due to the loss mode and back reflection present in the coupling process of the HPP sandwich structure. Subsequently, the power ratio Γ_{AL} for loss mode A_L with different thicknesses of silver plates is calculated based on eqn (2) (see Fig. S5 of the ESI†). The results show that the proportion of the loss mode first decreases and then increases with the increase of the silver plate thickness, which is consistent with the trend of the minimum transmission described in Fig. 7(b). Similarly, the calculated back reflection ratio Γ_R also follows the same trend, except that the proportion of reflection is the smallest at a thickness of 30 nm. Since the loss mode is mainly responsible

for the loss, the coupling efficiency of the device is maximized at a thickness of 30 nm, as shown in Fig. 7(c). This is because that it is much difficult to suppress radiation for a thin silver plate, but an overly thick plate will lead to excessive suppression, resulting in the inability to produce effective coupling between the photonic waveguide and the plasmonic structure. The maximum coupling efficiency of the device is $\sim 96\%$ at the thickness of 30 nm.

In addition, we also calculate the coupling efficiency of the PLSC with the width of the silicon photonic waveguide. As shown in Fig. 7(d), the coupling efficiency of the device increases and decreases periodically with the increase of the waveguide width, that is, when the waveguide width increases to 630 nm, the coupling efficiency of the device is $\sim 96.2\%$ and then falls. When the waveguide width is 740 nm, the coupling efficiency of the device is $\sim 95.9\%$ and then falls again. The maximum of the two coupling efficiencies corresponds to the matching condition being satisfied, while the lower maximum of the coupling efficiency is due to the appearance of higher order modes that dissipate a portion of the power in the waveguide.

The simulated electric-field distribution is shown in Fig. 8, where the TE-polarized light is launched from the left end of the device into the silicon photonic waveguide and then coupled into the hybrid photonic-plasmonic sandwich structure. As shown in Fig. 8(a), when the matching condition is satisfied, the device will use the hybrid photonic-plasmonic sandwich taper to realize the steering and focusing of the light. At the same time, almost no light waves are emitted from the other end of the waveguide. This result is due to the extreme coupling of the silicon photonic waveguide with the HPP sandwich structure. When the matching condition is not satisfied, as shown in Fig. 8(b), the light waves will be output directly from the other end *via* the silicon photonic waveguide without any priming effect, indicating that the silicon waveguide is not strongly coupled to the sandwich structure.

Nanofocusing ability of the designed PLSC

To understand the nanofocusing ability of PLSC in more detail, we have carried out numerical simulations for the on-chip taper with different apex angles. The tip of the silver taper is rounded to a curved surface with a radius of 15 nm.

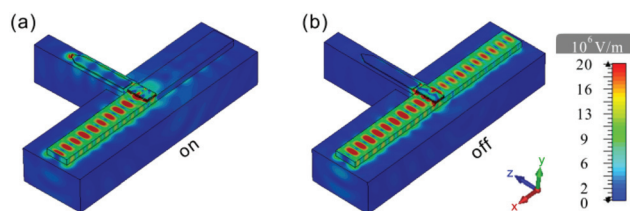


Fig. 8 (a) The electric-field distribution of PLSC when the matching condition is satisfied (a) and the matching condition is not satisfied (b). The wavelength is 1500 nm.

We use the enhancement factor of field amplitude to evaluate the nanofocusing performance of the device, which is defined as $|E|/|E_0|$. Here, $|E|$ is the maximum field amplitude at the apex and $|E_0|$ is the field amplitude of the photonic waveguide without the HPP structure. Fig. 9(a) shows the electric-field profiles at the $y = 0$ plane and at the $x = 0$ plane of the PLSC. It is shown that SPPs propagate along the edge of the silver taper towards the tip and eventually converged at the apex of the taper to achieve nanofocusing. Here, the taper angle is 6° . As shown in Fig. 9(a), the electric field is mainly confined to the substrate below the strip for the wide strip, because the refractive index of silica is larger than that of air. For the narrow strip close to the tip, the electric field is evenly distributed among the two materials, which is consistent with the effect produced by the nanofocusing devices in the free space studied by previous researchers.⁶ Fig. 9(b) shows the field amplitude enhancement factor at the apex of the taper as a function of the vertex angle. It can be seen from the figure that when the apex angle of the silver taper is 6° , the field amplitude at the tip is the largest, and the field amplitude enhancement factor is $\sim 7 \times 10^7$.

The adiabatic parameter, defined as $\delta(z) = |d(k(z))^{-1}/dz|$, is valid for a taper with an apex angle of 6° ,⁴⁶ where $k(z)$ is the wave vector of plasmons at propagation distance z . As shown by the blue line in Fig. 9(c), although the adiabatic parameter increases as the distance to the tip is gradually reduced, the condition of $\delta \ll 1$ is still satisfied, except in the vicinity of the tip. Thus, in the region of the taper that satisfies adiabatic

conditions, the SPPs can propagate along the edge of the metal waveguide without any radiation and back reflection. Previously, the mode analysis of tapered structures was performed by using the finite element method. As shown in Fig. 9(c), the effective mode index decreases gradually as the distance to the tip increases (*i.e.*, the strip width of the taper becomes wider). The coordinates of the horizontal dotted line represent the refractive index of silica, indicating that the strip width is infinite at this time. The inset shows the normalized electric-field amplitude profiles for the strip widths of 30 nm and 300 nm, and the electric-field vector indicated by the green arrow corresponds to the electric field distribution in Fig. 9(a). The group/phase velocity of the plasmon related to the effective mode index can be calculated to account for the nano-focusing effect. The group velocity of the plasmon is defined as $v_g = c[d(n\omega)/d\omega]^{-1}$, and the phase velocity of the plasmon is defined as $v_p = c/n$, which can be calculated under adiabatic conditions. As a result, the group/phase velocity of the plasmon decreases as the distance to the tip decreases until it reaches 0 at the apex of the taper.

Finally, we calculate the mode width w_{mode} for silver strips with different widths by measuring the full width at half maximum of the electric-field amplitude profile of the taper. As shown in Fig. 9(d), the mode width increases almost linearly with the increase of the strip width, and the minimum mode width is approximately 110 nm when the silver strip is 30 nm (at the apex of the taper). This result is similar to the previously reported results.⁶ The inset shows the normalized electric-field amplitude profiles corresponding to different silver strip widths. When the width of the silver strip is 30 nm, the amplitude profile is approximately a Gaussian distribution. When the width of the silver strip exceeds 100 nm, the amplitude profile shows two peaks, which means that the electric field gradually localizes at the edge of the strip as the width of the silver strip increases, which is consistent with the top view of electric-field distribution shown in Fig. 9(a).

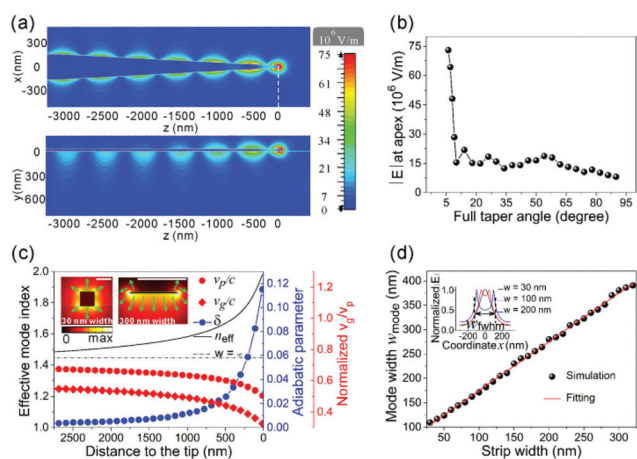


Fig. 9 The electric-field profiles at the $y = 0$ plane and at the $x = 0$ plane of the PLSC. The base width of the Ag taper is 300 nm, and the vertex angle is 6° . The radius of the curved surface at the tip is 15 nm, and the matching wavelength is 1500 nm. (b) The dependence of the field amplitude on the taper angle of the silver taper. (c) The dependence of group velocity v_g , phase velocity v_p , adiabatic parameter δ , and effective mode index on the distance to the tip of the silver taper. The inset shows the electric-field amplitude profiles of silver strip with widths of 30 nm and 300 nm. White bars correspond to 30 nm and 300 nm. The wavelength is 1500 nm. (d) The dependence of the mode width w_{mode} on the width of the silver strip. The inset shows the normalized amplitude profiles with different strip widths. The silver strip widths are 30 nm, 100 nm and 200 nm.

Conclusions

In conclusion, we have designed and systematically analysed an efficient on-chip plasmonic light steering concentrator (PLSC) consisting of a silicon photonic waveguide and a plasmonic sandwich taper structure. The fundamental quasi-TE mode light incident from the left end of the silicon waveguide generates two supermodes (quasi-TM modes) through the excitation of the hybrid photonic-plasmonic sandwich structure, thus realizing the steering and focusing of light waves. By optimizing the size parameters of this structure, the coupling efficiency of PLSC is as high as $\sim 96\%$, and a high extinction ratio of the specific wavelength light (1500 nm) is realized, which gives the device the mode selection function. In particular, the amplitude enhancement of the electric field of up to 10^7 is achieved at the apex of the radius of 15 nm compared to that of light in the photonic waveguide. The mode width of the field amplitude profile at the apex is laterally confined within

~110 nm, achieving a high degree of integration. This provides an opportunity for the application of integrated polarization-free photonic-plasmonic circuits.

Conflicts of interest

There are no conflicts to declare.

Acknowledgements

We are grateful for the financial support from the National Natural Science Foundation of China (61571242), the Fundamental Research Funds for the Central Universities of China, and the National Creative Research Laboratory program (Grant no. 2012026372) through the National Research Foundation of Korea.

Notes and references

- J. A. Schuller, E. S. Barnard, W. S. Cai, Y. C. Jun, J. S. White and M. L. Brongersma, *Nat. Mater.*, 2010, **9**, 193–204.
- K. M. Mayer and J. H. Hafner, *Chem. Rev.*, 2011, **111**, 3828–3857.
- W. L. Barnes, A. Dereux and T. W. Ebbesen, *Nature*, 2003, **424**, 824–830.
- D. K. Gramotnev and S. I. Bozhevolnyi, *Nat. Photonics*, 2010, **4**, 83–91.
- D. K. Gramotnev and S. I. Bozhevolnyi, *Nat. Photonics*, 2014, **8**, 14–23.
- V. A. Zenin, A. Andryieuski, R. Malureanu, I. P. Radko, V. S. Volkov, D. K. Gramotnev, A. V. Lavrinenko and S. I. Bozhevolnyi, *Nano Lett.*, 2015, **15**, 8148–8154.
- K. Wang, E. Schonbrun, P. Steinvurzel and K. B. Crozier, *Nano Lett.*, 2010, **10**, 3506–3511.
- P. Neutens, P. V. Dorpe, I. D. Vlaminc, L. Lagae and G. Borghs, *Nat. Photonics*, 2009, **3**, 283–286.
- R. F. Oulton, V. J. Sorger, T. Zentgraf, R. Ma, C. Gladden, L. Dai, G. Bartal and X. Zhang, *Nature*, 2009, **461**, 629–632.
- P. R. West, S. Ishii, G. Naik, N. Emani, V. M. Shalaev and A. Boltasseva, *Laser Photonics Rev.*, 2010, **4**, 795–808.
- J. N. Anker, W. P. Hall, O. Lyandres, N. C. Shah, J. Zhao and R. P. Van Duyne, *Nat. Mater.*, 2008, **7**, 442–453.
- P. Bharadwaj, B. Deutsch and L. Novotny, *Adv. Opt. Photonics*, 2009, **1**, 438–483.
- K. A. Willets and R. P. Van Duyne, *Annu. Rev. Phys. Chem.*, 2007, **58**, 267–297.
- N. J. Halas, S. Lal, W.-S. Chang, S. Link and P. Nordlander, *Chem. Rev.*, 2011, **111**, 3913–3961.
- S. M. Stranahan and K. A. Willets, *Nano Lett.*, 2010, **10**, 3777–3784.
- D. Punj, M. Mivelle, S. B. Moparthy, T. S. van Zanten, H. Rigneault, N. F. van Hulst, M. F. García-Parajó and J. Wenger, *Nat. Nanotechnol.*, 2013, **8**, 512–516.
- M.-K. Kim, H. Sim, S. J. Yoon, S.-H. Gong, C. W. Ahn, Y.-H. Cho and Y.-H. Lee, *Nano Lett.*, 2015, **15**, 4102–4107.
- S. Kim, J. Jin, Y.-J. Kim, I.-Y. Park, Y. Kim and S.-W. Kim, *Nature*, 2008, **453**, 757–760.
- A. D. McFarland and R. P. Van Duyne, *Nano Lett.*, 2003, **3**, 1057–1062.
- D. Dai and S. He, *Opt. Express*, 2009, **17**, 16646–16653.
- Y. Song, J. Wang, Q. Li, M. Yan and M. Qiu, *Opt. Express*, 2010, **18**, 13173–13179.
- R. M. Briggs, J. Grandidier, S. P. Burgos, E. Feigenbaum and H. A. Atwater, *Nano Lett.*, 2010, **10**, 4851–4857.
- V. J. Sorger, Z. Ye, R. F. Oulton, Y. Wang, G. Bartal, X. Yin and X. Zhang, *Nat. Commun.*, 2011, **2**, 331.
- X. He, L. Yang and T. Yang, *Opt. Express*, 2011, **9**, 12865–12872.
- M. Chamanzar and A. Adibi, *Opt. Express*, 2011, **19**, 22292–22304.
- M. Février, P. Gogol, A. Aassime, R. Mégy, C. Delacour, A. Chelnokov, A. Apuzzo, S. Blaize, J.-M. Lourtioz and B. Dagens, *Nano Lett.*, 2012, **12**, 1032–1037.
- F. B. Arango, A. Kwadrin and A. F. Koenderink, *ACS Nano*, 2012, **6**, 10156–10167.
- X. Wu, Y. Xiao, C. Meng, X. Zhang, S. Yu, Y. Wang, C. Yang, X. Guo, C. Z. Ning and L. Tong, *Nano Lett.*, 2013, **13**, 5654–5659.
- M. Chamanzar, Z. Xia, S. Yegnanarayanan and A. Adibi, *Opt. Express*, 2013, **21**, 32086–32098.
- G. D. Osowiecki, E. Barakat, A. Naqavi and H. P. Herzig, *Opt. Express*, 2014, **22**, 20871–20880.
- Y. Luo, M. Chamanzar, A. Apuzzo, R. Salas-Montiel, K. N. Nguyen, S. Blaize and A. Adibi, *Nano Lett.*, 2015, **15**, 849–856.
- F. Peyskens, A. Z. Subramanian, P. Neutens, A. Dhakal, P. V. Dorpe, N. L. Thomas and R. Baets, *Opt. Express*, 2015, **23**, 3088–3101.
- S. Kim and M. Qi, *Opt. Express*, 2015, **23**, 9968–9978.
- L. Gao, Y. Huo, K. Zang, S. Paik, Y. Chen, J. S. Harris and Z. Zhou, *Sci. Rep.*, 2015, **5**, 15794.
- Y.-H. Jin, B. J. Park and M.-K. Kim, *Opt. Express*, 2016, **24**, 25540–25547.
- P. C. Wuytens, A. G. Skirtach and R. Baets, *Opt. Express*, 2017, **25**, 12926–12934.
- S. P. Zhang and H. X. Xu, *ACS Nano*, 2012, **6**, 8128–8135.
- Y. S. Bian and Q. H. Gong, *Nanoscale*, 2015, **7**, 4415–4422.
- P. B. Johnson and R. W. Christy, *Phys. Rev. B: Solid State*, 1972, **6**, 4370–4379.
- K. C. Vernon, A. M. Funston, C. Novo, D. E. Gómez, P. Mulvaney and T. J. Davis, *Nano Lett.*, 2010, **10**, 2080–2086.
- M. A. Green, *Sol. Energy Mater. Sol. Cells*, 2008, **92**, 1305–1310.
- L. H. Gao, F. Lemarchand and M. Lequime, *Opt. Express*, 2012, **20**, 15734–15751.
- W.-P. Huang, *J. Opt. Soc. Am. A*, 1994, **11**, 963–983.
- J. Homola, *Chem. Rev.*, 2008, **108**, 462–493.
- J. D. Jackson, *Classical Electrodynamics*, Wiley & Sons, New York, 1975.
- M. I. Stockman, *Phys. Rev. Lett.*, 2004, **93**, 137404.